RSC Advances

PAPER

View Article Online
View Journal | View Issue

Cite this: *RSC Adv.*, 2023, **13**, 18816

Oxygen functionalized InSe and TlTe two-dimensional materials: transition from tunable bandgap semiconductors to quantum spin Hall insulators†

Qing Lu, [a] Lin Li,[a] Shilin Luo,[a] Yue Wang,[a] Busheng Wang *[b] and Fu-Ti Liu*[a]

From first-principles calculations, we found that oxygen functionalized InSe and TlTe two-dimensional materials undergo the following changes with the increased concentrations of oxygen coverage, transforming from indirect bandgap semiconductors to direct bandgap semiconductors with tunable bandgap, and finally becoming quantum spin hall insulators. The maximal nontrivial bandgap are 0.121 and 0.169 eV, respectively, which occur at 100% oxygen coverage and are suitable for applications at room temperature. In addition, the topological phases are derived from SOC induced p–p bandgap opening, which can be further determined by Z_2 topological invariants and topologically protected gapless edge states. Significantly, the topological phases can be maintained in excess of 75% oxygen coverage and are robust against external strain, making the quantum spin hall effect easy to achieve experimentally. Thus, the oxygen functionalized InSe and TlTe are fine candidate materials for the design and fabrication of topological devices.

Received 16th April 2023
Accepted 14th June 2023

DOI: 10.1039/d3ra02518g

rsc.li/rsc-advances

1. Introduction

Group III sulfur compound layered materials have become a research hotspot[1,2] due to their high carrier mobility, p-type electronic behavior and wide-cap shaped band edges. Their layered or monolayer materials (GaS, GaSe and InSe) have been experimentally realized,[3–5] forming a new class of two-dimensional (2D) materials. These 2D materials can be used as candidates for optoelectronic devices and electronic devices,[6–8] where field effect transistors made with monolayer InSe have high carrier mobility and large switching ratio,[6,7] photodetectors made with GaS,[4] GaSe,[5] GaTe,[9] InSe[10] and TlTe[11] show high photoresponsiveness and fast response time. In addition, these 2D materials have potential applications in thermoelectric,[12] piezoelectric[13] and electrocatalytic fields.[14]

Quantum spin hall (QSH) insulators, which is called 2D topological insulators, was first proposed in graphene[15,16] and then experimentally achieved in HgTe/CdTe[17,18] and InAs/GaSb[19,20] quantum wells. Chemically functionalized 2D materials are an effective way to modulate structural and electronic properties.[21–24] Halogenation, hydrogenation, methyl and ethynyl functionalization, oxidation of 2D materials have been studied in theoretical detail, with tunable electronic and topological properties. With halogenation and hydrogenation, germanene,[25,26] stanene,[26–28] phosphene,[29] arsenene,[30,31] antimonene[32] and bismuthene[33] as well as binary compounds with inversion asymmetry[31,34–40] are 2D topological insulators with large bandgap, with the largest bandgap reaching 1.08 eV. In addition, methyl functionalized stanene,[41,42] arsenene[43] and bismuthene,[44] as well as ethynyl functionalized stanene[45] can further improve the nontrivial topological bandgap. Finally, with oxygen functionalization, arsenene,[46] antimonene[47] and bismuthene[48] can also achieve QSH insulators with large bandgap. All of these topological insulators have the potential for room-temperature applications.

Despite the considerable properties of group III sulfur compounds, few studies have focused on their chemical modification. Oxidized InSe monolayer by heat treatment, Balakrishnan *et al.* obtained the InSe/In_2O_3 heterojunction and found that it could be used as a p–n junction with tunable bandgap.[49] Researchers have also found that oxidized GaSe and GaTe films could lead to a decrease in photoluminescence.[50,51] Monolayer InSe has rich electronic and optical properties, which can obtain nontrivial topological phases through full oxygen coverage.[52] Considering that partial oxygen coverage may occur under experimental conditions, it is of great significance to study the electronic and topological properties of InSe 2D materials with different concentrations of oxygen coverage. Among the group III elements, Tl and Te elements have stronger spin–orbit coupling (SOC) than In and Se elements, respectively,

[a]*Key Laboratory of Computational Physics of Sichuan Province, Faculty of Science, Yibin University, Yibin 644000, China. E-mail: futiliu@163.com*

[b]*Department of Chemistry, State University of New York at Buffalo, Buffalo, NY 14260-3000, USA. E-mail: bushengw@buffalo.edu*

† Electronic supplementary information (ESI) available. See DOI: https://doi.org/10.1039/d3ra02518g

and should be able to further induce and stabilize their topological phases.

In this paper, we have studied InSe and TlTe 2D materials with different concentrations of oxygen coverage through 2×2 supercell. The InSe changes from an indirect bandgap semiconductor to a direct bandgap semiconductor at 25% oxygen coverage ($InSeO_{0.25}$), and the bandgap is decreased from 1.392 eV to 0.636 eV. The InSe also keeps a direct bandgap semiconductor at 50% oxygen coverage ($InSeO_{0.5}$) with the bandgap further reduced to 0.123 eV, transforming into a QSH insulator at 75% oxygen coverage ($InSeO_{0.75}$). The 2D material InSe at 100% oxygen coverage, namely InSeO, has a nontrivial bandgap of 0.121 eV, which is suitable for applications at room temperature. The oxygen functionalized TlTe shows the same trend as the oxygen functionalized InSe. With the increased concentrations of oxygen coverage, the TlTe changes from an indirect bandgap semiconductor to a direct bandgap semiconductor, and turns into a QSH insulator at 75% oxygen coverage ($TlTeO_{0.75}$). The TlTe 2D material at 100% oxygen coverage (TlTeO) has a nontrivial bandgap increased to 0.169 eV due to the strong SOC of Tl elements. Their topological phases are derived from SOC-induced p–p bandgap opening and can be further determined by Z_2 topological invariants and topologically protected gapless edge states.

2. Theoretical methods and computational details

First-principles calculations were performed using the projected augmented wave (PAW) method[53] as implemented in the Vienna *ab initio* simulation package (VASP).[54] The exchange-correlation energy was treated using Perdew–Burke–Ernzerhof (PBE)[55] generalized gradient approximation. The energy cutoff of the plane wave basis was selected as 500 eV with an energy precision of 10^{-5} eV. Meanwhile, $11 \times 11 \times 1$ *K* point grid[56] was selected for Brillouin-zone sampling. All atoms are relaxed until the force on each atom is lower than 0.01 eV $Å^{-1}$. The setting of these parameters is sufficient to ensure the accuracy of structure optimization. For self-consistent and energy band calculations, the energy cutoff of plane wave basis was remained as 500 eV, with energy precision improved to 10^{-6} eV, and the Brillouin-zone sampling was increased to $15 \times 15 \times 1$ *K* point grid. The influence of SOC was taken into account in all the processes starting from static self-consistent calculation. Phonopy[57] based on density functional perturbation theory was used to calculate the phonon spectra. The Wannier90 function[58] combined with WannierTools[59] was used to calculate the topological invariant Z_2 and topologically protected edge states.

3. Results and discussion

3.1 Crystal and electronic structures of oxygen functionalized InSe

The crystal of InSe contains two layers of In atoms between two layers of Se atoms, which can be regarded as two layers of InSe with hexagonal honeycomb shape connected by In atoms, as shown in Fig. 1(a). Therefore, an InSe primitive cell contains two In and Se atoms. After structure optimization, the lattice constant *a*, the bond length d_{In-Se} formed by In and Se atoms, and the bond length d_{In-In} formed between In atoms are 4.085, 2.682 and 2.824 Å, respectively. The calculated band structure of InSe is shown in Fig. 1(b). It is obvious that the valence band top is located between *Γ* and *K* points, while the conduction band bottom is located at *Γ* point, forming an indirect bandgap of 1.392 eV, which has the characteristics of semiconductor. In addition, the valence band top and the conduction band bottom have a wide brimmed hat and a parabolic shape, respectively. By constructing 2×2 supercells of InSe, and adsorbing O atoms simultaneously on Se atoms at both ends, we can study the effect of oxygen coverage at different concentrations.

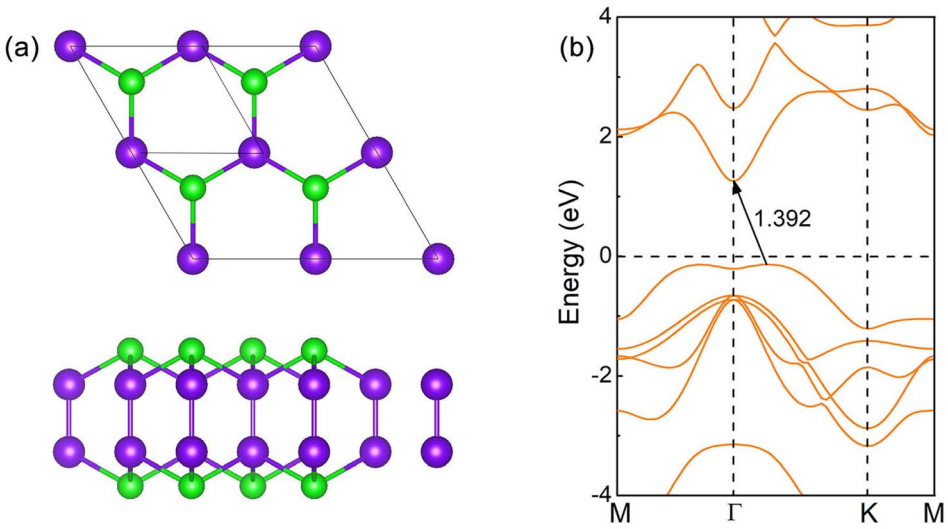

Fig. 1 (a) Top view and side view of the structure of InSe 2D material. The blue and green spheres represent In and Se atoms, respectively. The small square represents one of the primitive cells. (b) The band structure of InSe with the bandgap size.

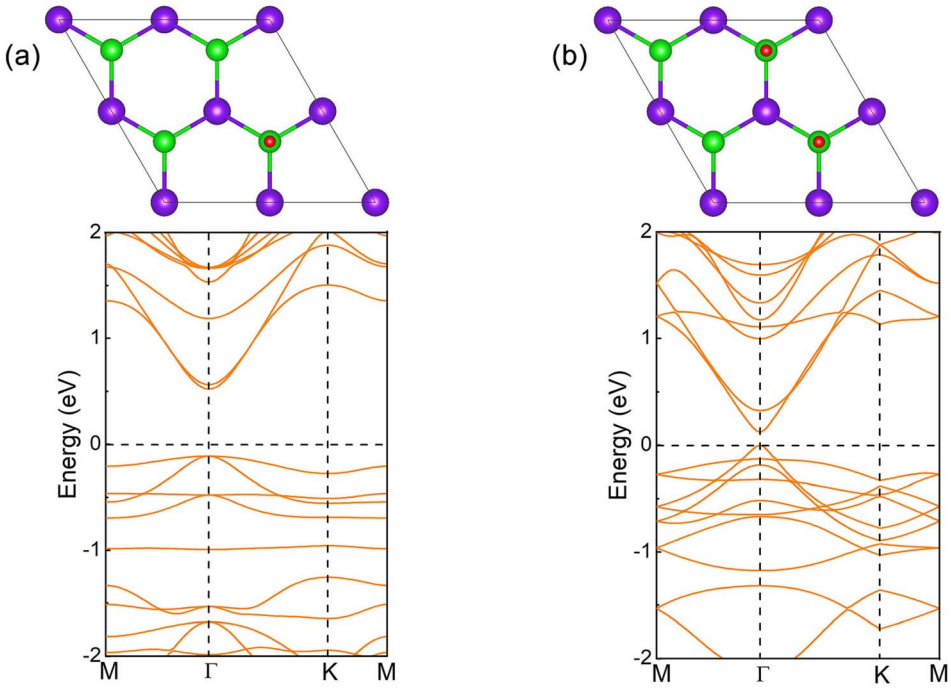

Fig. 2 Top view and calculated band structure of the oxygen functionalized InSe. (a) $InSeO_{0.25}$, and (b) $InSeO_{0.5}$. The blue, green and red balls represent In, Se and O atoms respectively.

The structure and band structure of InSe at 25% oxygen coverage ($InSeO_{0.25}$) are shown in Fig. 2(a). Compared with InSe, we adsorb O atoms simultaneously on Se atoms at both ends of a single cell. After structure optimization, the lattice constant a and the bond length d_{Se-O} of $InSeO_{0.25}$ are 8.263 and 1.679 Å, respectively, as shown in Table 1. The band structure of $InSeO_{0.25}$ changes from indirect bandgap to direct bandgap with the bandgap also decreasing from 1.392 eV to 0.636 eV. For InSe 2D materials at 50% oxygen coverage ($InSeO_{0.5}$), we adsorbed O atoms simultaneously on Se atoms at both ends of two single cells. After structure optimization, the lattice constant a of $InSeO_{0.5}$ is 8.423 Å and the bond length d_{Se-O} formed by Se and O atoms is 1.688 Å. The $InSeO_{0.5}$ 2D material is still a direct bandgap semiconductor with the bandgap further reduced to 0.123 eV, as shown in Fig. 2(b).

For InSe 2D material at 75% oxygen coverage ($InSeO_{0.75}$), we adsorbed O atoms simultaneously on Se atoms at both ends of three single cells. After structure optimization, the lattice constant a of $InSeO_{0.75}$ is 8.67 Å and the bond length d_{Se-O} formed by Se and O atoms is 1.683 Å, as shown in Table 1. From the band structure and the orbital projection band structure of $InSeO_{0.75}$, it can be seen that the two $p_{x,y}$ orbitals are degenerated at the Γ point of Fermi level and occupy the conduction band bottom and the valence band top, showing the gapless semi-metallic characteristics in the absence of SOC. After considering the SOC, the two degenerate $p_{x,y}$ orbitals are split apart, with one degenerate $p_{x,y}$ orbital moving up, the other degenerate $p_{x,y}$ orbital moving down, as shown in Fig. 3(a) and 4(a). Thus, the SOC induced p–p bandgap opening occurs in $InSeO_{0.75}$. Both $p_{x,y}$ orbitals exhibit parabolic quasi-quadratic dispersion relations and there are still very few s and p_z orbitals above and below the two $p_{x,y}$ orbitals.

Table 1 After structure optimization, the lattice constant a and the bond length d_{Se-O} of the oxygen functionalized InSe

	$InSeO_{0.25}$	$InSeO_{0.50}$	$InSeO_{0.75}$	InSeO
a	8.263	8.423	8.67	4.478
d_{Se-O}	1.679	1.688	1.683	1.68

For InSe 2D material at 100% oxygen coverage (InSeO), O atoms are simultaneously adsorbed on Se atoms at both ends of four single cells. However, a single cell is still used in the calculation. The lattice constant a of the optimized InSeO, the bond lengths d_{In-Se} formed by In atoms and Se atoms, and the bond lengths d_{In-In} formed between In atoms are increased to 4.478, 2.826 and 2.931 Å. The bond formed by Se and O atoms is perpendicular to InSe to reduce the influence of Coulomb repulsion. The bond length d_{Se-O} is 1.68 Å, and the corresponding bond overlap number is 0.58, indicating that Se and O atoms are covalently bonded. Just like $InSeO_{0.75}$, when SOC is not considered, two degenerate $p_{x,y}$ orbitals occupy the Fermi level, showing the gapless semi-metallic characteristics. After considering the SOC, the two degenerate $p_{x,y}$ orbitals are split, and p–p bandgap opening appears, as shown in Fig. 3(b) and 4(b). The parabolic shape of the two $p_{x,y}$ orbitals is much more pronounced, and there are also very few s and p_z orbitals above and below the two $p_{x,y}$ orbitals.

Wang *et al.* used the three orbitals s, p_x and p_y as the minimum basis to construct tight-binding model in triangular lattice.[60] They confirmed that QSH phase can originate from two

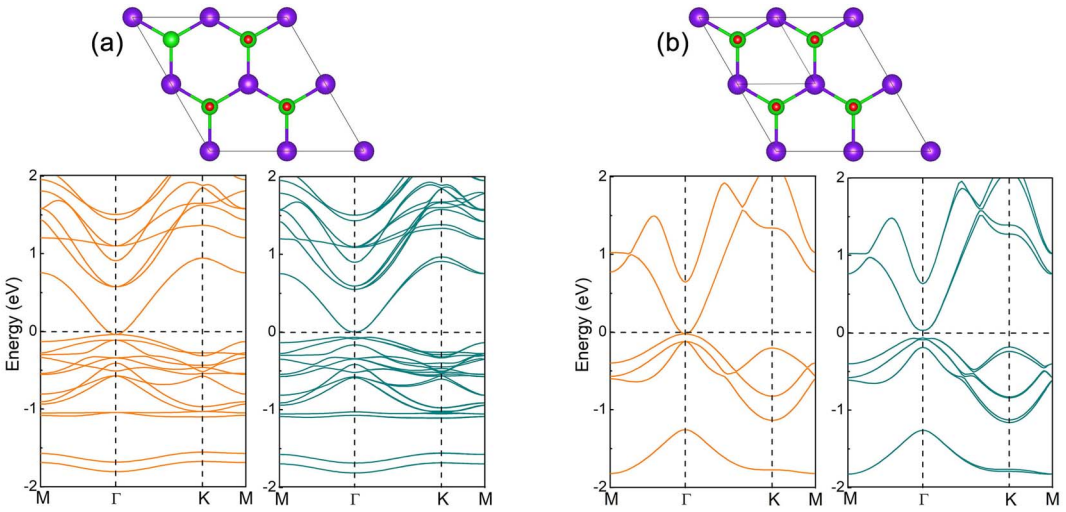

Fig. 3 Structure and band structure of (a) $InSeO_{0.75}$ and (b) InSeO. Orange and dark gray curves represent the band structures without and with SOC, respectively. The blue, green and red balls represent In, Se and O atoms respectively.

mechanisms, namely, SOC induced s–p band inversion or SOC induced p–p bandgap opening. For the first mechanism, the s orbital is above the p orbital, and after considering the SOC, a degenerate p and s orbital are reversed, resulting in the formation of the QSH phase. For the second mechanism, the p orbitals are degenerated at the Γ point, and when SOC is taken into account, the p–p bandgap opens and the QSH phase is generated. The second mechanism was also proposed by Liang *et al.*[61] They used multiple p orbitals, mainly p_x and p_y orbitals, to construct the $k \cdot p$ model, and proved that multiple p orbitals would exhibit degenerate and quasi-quadratic band dispersion at Γ point, and when SOC is included, the p–p bandgap would open and generate nontrivial topological phase. Thus, for $InSeO_{0.75}$ and InSeO 2D materials, their QSH phases arise from SOC induced p–p bandgap opening. The systems with the same mechanism include Au on GaAs(1 1 1) surface,[60] Bi on Si(1 1 1) surface, Bi-AU-H on SiC(1 1 1) surface[61] and Bi/Ag on Si(1 1 1) surface.[62] The nontrivial bandgap of InSeO is 0.097 eV, which is sufficient for room temperature applications. As the PBE functional[55] usually underestimate the bandgap, the HSE06 functional[63] is employed to correct the bandgap. In the absence of SOC, the InSeO maintains semi-metallic characteristics with HSE06. After considering the SOC, the nontrivial band gap of InSeO is increased to 0.121 eV, as shown in Fig. S1.† We also employ G_0W_0 method[21–24] to calculate the band gap of InSeO, which further increased to 0.351 eV.

Oxygen functionalized InSe provide the opportunity to modulate the band gap. To reveal the origin of these electronic properties, we examine the partial charge densities of the functionalized InSe, as illustrated in Fig. S2.† Pristine InSe have

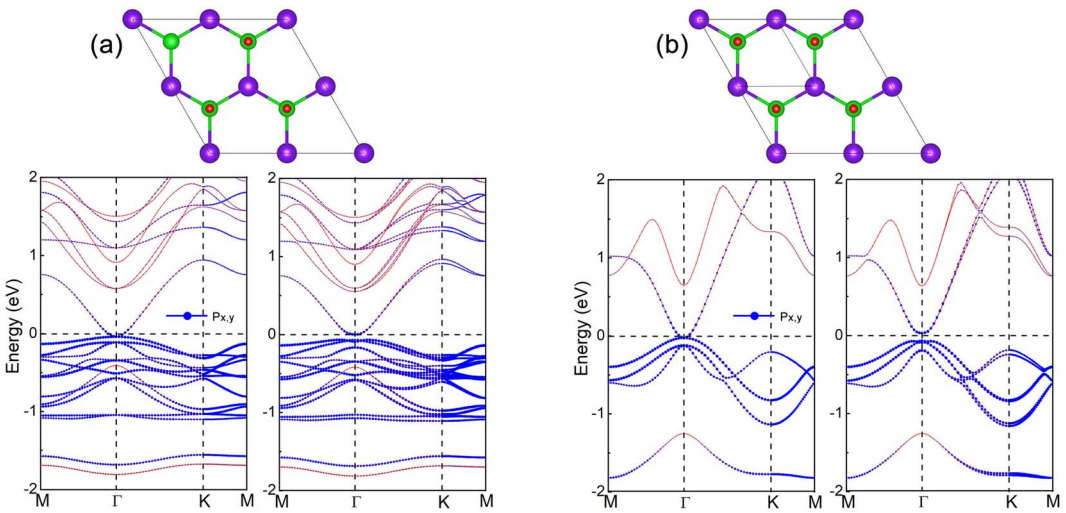

Fig. 4 Structure and orbital projected band structure of (a) $InSeO_{0.75}$ and (b) InSeO. The left and right sides represent the band structures without and with SOC, respectively. The blue circle represents the $p_{x,y}$ orbitals, with the size of the circle corresponding to the weight of the projected orbit.

the top valence band (VB) originated from the p_z orbitals of In and Se atoms, and the bottom conduction band (CB) dominated by the s orbitals of both atoms. Accordingly, the top VB charge densities exhibit the p_z orbital character, while the bottom CB charge densities are accumulated in between the In and Se atoms showing the in-plane σ bond character. In contrast, InSeO monolayers have the top VB and bottom CB both dominated by the p_x and p_y orbitals of In, Se, and O atoms. The partial charge densities of the bands are localized individually on the Se and O atoms, indicating the occupancy of antibonding states between Se and O atoms that leads to the narrowing of band gap.

We use the following formula to calculate the formation energy of InSeO : $E_f = E(\text{InSeO}) - E(\text{InSe}) + E(\text{O})$, where E(InSeO) is the total energy of InSeO, E(InSe) is the total energy of InSe, and E(O) is the chemical potential of O atom. The calculated formation energy for InSeO is −2.774 eV. Therefore, O atoms are strongly bound to InSe through chemical bonding, and InSeO exhibit high thermodynamic stability. Correspondingly, the $InSeO_{0.25}$, $InSeO_{0.5}$ and $InSeO_{0.75}$ are also thermodynamically stable. In Fig. 5, the phonon spectra of InSe and InSeO are also calculated. It can be seen that although the InSe has been synthesized experimentally, there is still a little virtual frequency at its Γ point. However, InSeO has no virtual frequency in the whole Brillouin area, which indicates that InSeO is dynamically stable. Therefore, the stability of InSe 2D material can be improved by oxygen functionalization. To further inspect the thermal stability of InSeO, we carry out *ab initio* molecular dynamics simulations (MD) with 4 × 4 × 1 supercell. The snapshot of atomic configuration at 300 K is plotted for InSeO at 2 ps, as illustrated in Fig. S3.† Neither structure reconstruction nor structure disruption appeared in InSeO, indicating that InSeO possess good thermal stability and maintains structural integrity at room-temperature. Like oxygen functionalized graphene,[64] oxygen functionalized InSe 2D materials also hold great promise for synthesis by oxygen plasma technology.

3.2 Crystal and electronic structures of oxygen functionalized TlTe

After structure optimization, the lattice constant a of TlTe 2D material is 4.535 Å, the bond length $d_{\text{Tl–Te}}$ formed by Tl atoms and neighboring Te atoms and the bond length $d_{\text{Tl–Tl}}$ formed between the upper and lower layers of Tl atoms are 2.963 and 2.922 Å, respectively. The calculated band structure is shown in Fig. 6(a), same as InSe, the valence band top is located between the Γ and K points, and the conduction band bottom is located at Γ point, forming an indirect bandgap of 0.433 eV with a semiconductor characteristic.

For TlTe at 50% oxygen coverage ($TlTeO_{0.5}$), the lattice constant a and the bond length $d_{\text{Te–O}}$ formed by Te and O atoms are 9.4 and 1.854 Å, respectively. The bandgap of $TlTeO_{0.50}$ changes from the indirect bandgap to the direct bandgap, and the bandgap also decreases from 0.433 eV to 0.152 eV, as shown in Fig. 6(b). For TlTe 2D material at 100% oxygen coverage (TlTeO), the lattice constant a, the bond length $d_{\text{Te–O}}$ of Te and O atoms, the bond length $d_{\text{Tl–Te}}$ of Tl atoms and neighboring Te atoms, and the bond length $d_{\text{Tl–Tl}}$ between the upper and lower layers of the Tl atoms are 5.032, 1.848, 3.135 and 3.104 Å, respectively. When the SOC is not considered, the two $p_{x,y}$ orbitals are degenerated at the Fermi level Γ point, exhibiting the semi-metallic characteristics. After considering the SOC, two degenerate $p_{x,y}$ orbitals are split apart, accompanied by the p–p bandgap opening, as shown in Fig. 6(c), indicating that TlTeO is the QSH insulator. Since the SOC intensity of Tl is larger than that of In, the nontrivial bandgap of TlTeO is increased to 0.124 eV by PBE functional[55] (or 0.169 eV by HSE06 functional[63]), which has the more potential to be applied at room temperature, as shown in Fig. S1.† In fact, TlTe also become QSH insulator at 75% oxygen coverage ($TlTeO_{0.75}$). However, the bandgap induced by the SOC is extremely small, which is easily destroyed by the thermally excited charge carriers. Thus, in terms of device application, it is better to choose the TlTeO. The calculated formation energy of TlTeO is −3.98 eV, which is larger than that of InSeO. It also shows great

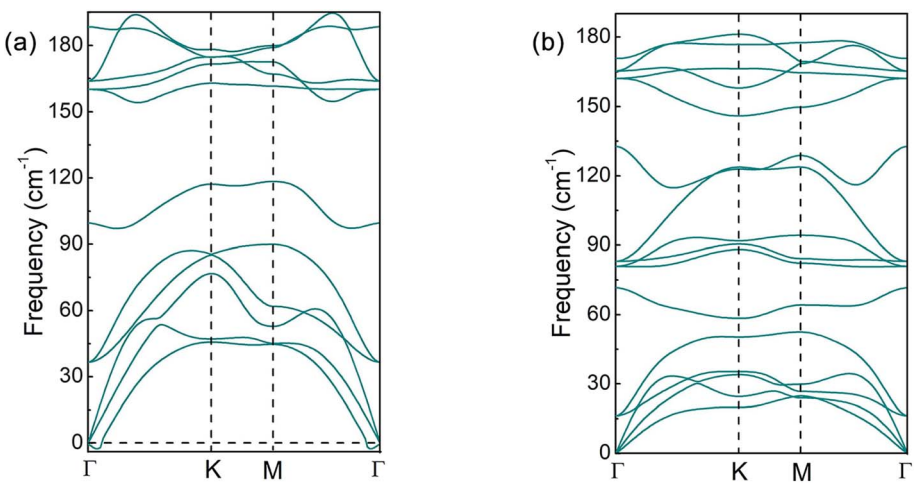

Fig. 5 Phonon spectrum of (a) InSe and (b) InSeO.

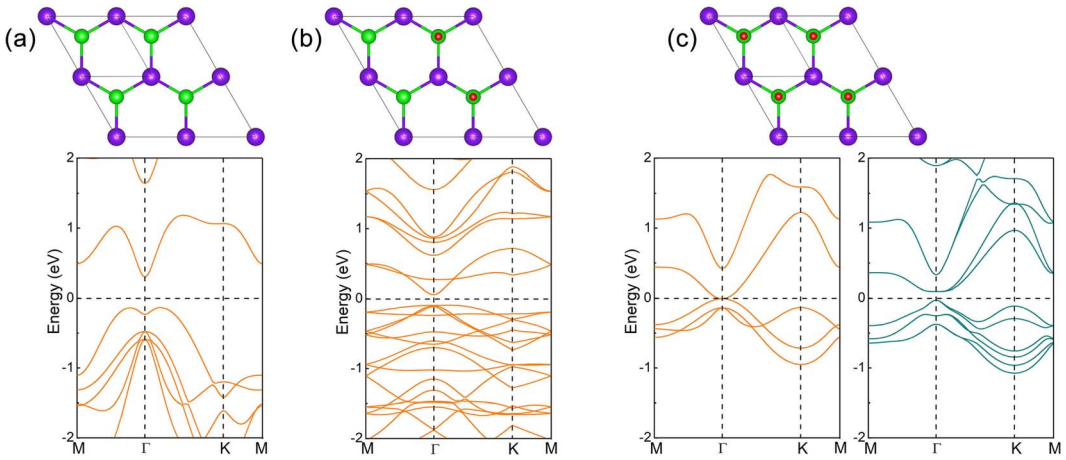

Fig. 6 Structure and band structure of (a) TlTe, (b) $TlTeO_{0.5}$ and (c) TlTeO. Orange and dark gray curves represent the band structures without and with SOC, respectively. The blue, green and red balls represent Tl, Te and O atoms, respectively.

thermodynamic stability, so TlTeO has great hope of being synthesized by oxygen plasma technology.[64] The snapshot of atomic configuration at 300 K is also plotted for TlTeO, as illustrated in Fig. S3.† Neither structure reconstruction nor structure disruption appeared in TlTeO.

3.3 Z_2 topological invariants and topologically protected edge states

The topological properties of 2D materials can be determined by Z_2 topological invariants and topologically protected edge states. In orbital projection, p_x and p_y orbitals have a great influence on the energy bands close to the Fermi level and the topological properties of the system, which are must be considered. However, there are still a small number of s and p_z orbitals in the selected energy range, which will affect the overall smoothness of the projected bands, and should also be considered. After the projection orbitals are set, the Wannier90 function[58] combined with VASP[53] is used to calculate and generate Wannier function. By adjusting the freezing window, resolving entanglement window and related parameters, a good tight-binding model will be acquired. Finally, the obtained tight-binding model is brought into the WannierTools[59] for calculation.

Using WannierTools software to calculate the evolution of Wannier Charge Center (WCC),[65] Z_2 topological invariants can be obtained to identify the topological states. For InSeO and TlTeO 2D materials, the calculated Z_2 topological invariants are 1, which confirms that they are both QSH insulators. The topologically protected edge states in bulk gap are also intuitive representations of the topological properties. Using iterative Green's function[59] embedded in the WannierTools, we can obtain topologically protected edge states of InSeO and TlTeO, as shown in Fig. 7(a) and (b). Their edge states connect the valence and conduction bands and cross the Fermi level from X point to G point odd number of times, further confirming that InSeO and TlTeO are QSH insulators. These edge states are protected from backscattering by time-inversion symmetry and can ensure non-dissipative electron transport.[62]

3.4 Bandgap variation and orbital evolution under strain

Strains can effectively regulate the electronic and topological properties of 2D materials.[66–73] The strains in InSeO and TlTeO can be defined as $\varepsilon = (a - a_0)/a_0$, where a_0 and a denote lattice constants at equilibrium and under strains, respectively. The changes of the bandgap E_I-with and E_g-with under strains are shown in Fig. 8(a) and (b), where E_I-with represents the direct

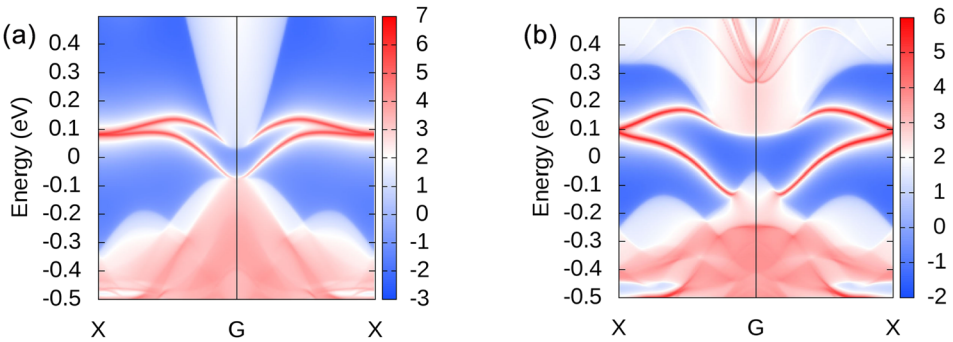

Fig. 7 Topologically protected edge states of (a) InSeO and (b) TlTeO.

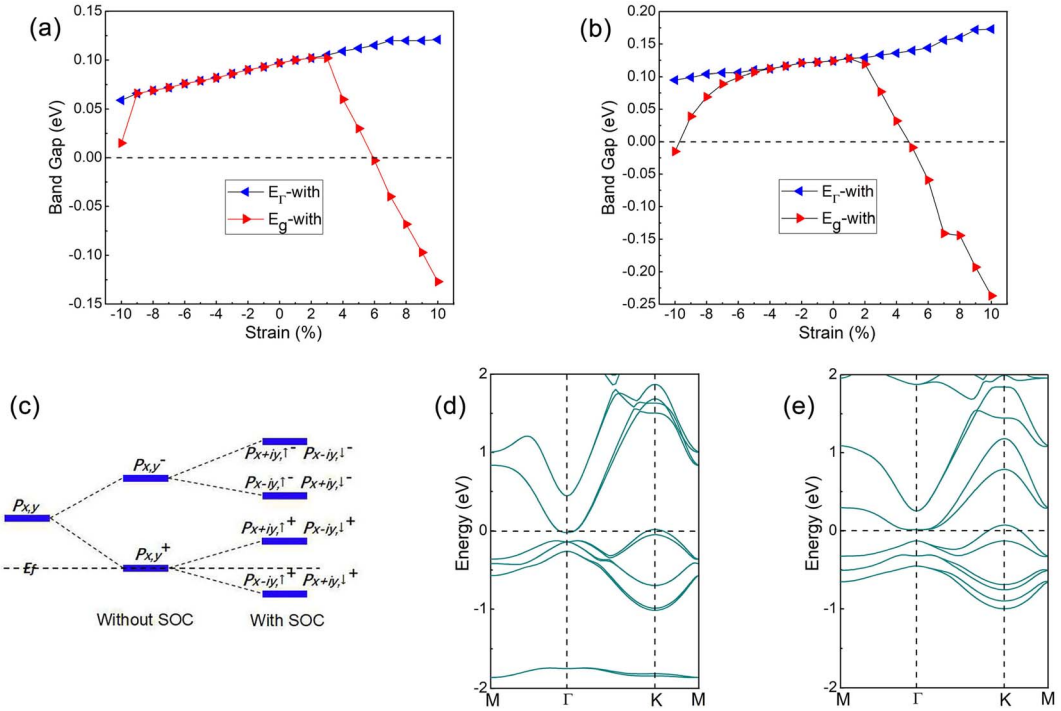

Fig. 8 The bandgaps E_I-with and E_g-with of (a) InSeO and (b) TlTeO change with strain. E_I-with represents the direct bandgap at the Γ point under SOC and E_g-with represents the global bandgap under SOC. (c) Orbital evolution of InSeO and TlTeO under strain. (d) Band structure of InSeO at 7% tensile strain considering the SOC. (e) Band structure of TlTeO at 6% tensile strain considering the SOC.

bandgap at the Γ point under SOC and E_g-with represents the global bandgap under SOC. For InSeO, E_I-with increases slowly with strains and reaches a maximum value of 0.121 eV at 7% strain. E_g-with increases monotonically with strains at first, reaches a maximum value of 0.102 eV at 3% strain, and then decreases monotonically with strains. The E_I-with and E_g-with are consistent at −9% to 2% strains, and the band of InSeO shows a direct bandgap. Under other strains, the E_I-with and E_g-with are separated from each other, and the band of InSeO appears as an indirect bandgap. When the strains are greater than 6%, the value of E_g-with is less than 0, and InSeO exhibits semi-metallic characteristics. For TlTeO, E_I-with and E_g-with show the same trend as InSeO. The maximum value of E_I-with is 0.172 eV at 9% strain, and the maximum value of E_g-with is 0.128 eV at 1% strain. The E_I-with and E_g-with are consistent under strains of −4% to 1%, and the band of TlTeO shows a direct bandgap. When the applied strains are greater than 5%, the value of E_g-with is less than 0, and TlTeO exhibits semi-metallic characteristics.

Next, we will analyze the evolution of orbitals under strains. Since O atoms hybridize with p_z orbitals in the same energy range, p_z orbitals leave the Fermi level, so $p_{x,y}$ orbitals are mainly left around the Fermi level. Chemical bonding causes $p_{x,y}$ orbitals to split into bonded and antibonded states $|p_{x,y}^{\pm}\rangle$, where ± represents the bonded and antibonded states, respectively. When SOC is not considered, the $|p_{x,y}^{+}\rangle$ state are occupied at the Fermi level, exhibiting semi-metallic characteristics. After considering the SOC, the $|p_{x,y}^{+}\rangle$ are further split into $|p_{x+iy,\uparrow}^{+}, p_{x-iy,\downarrow}^{+}\rangle$ and $|p_{x-iy,\uparrow}^{+}, p_{x+iy,\downarrow}^{+}\rangle$, with $|p_{x+iy,\uparrow}^{+}, p_{x-iy,\downarrow}^{+}\rangle$ moving up and $|p_{x-iy,\uparrow}^{+}, p_{x+iy,\downarrow}^{+}\rangle$ moving down, so that a large energy gap opens and the QSH phase is generated, as shown in Fig. 8(c). It is obvious that once the SOC is taken into account, the p–p bandgap can be opened, with the generation of QSH phase. However, when the applied strains are greater than 6% and 5%, respectively, the valence band top at point K rises above the Fermi level, so that InSeO and TlTeO become semi-metallic again, as shown in Fig. 8(d) and (e).

4. Conclusions

By constructing InSe and TlTe 2 × 2 supercells, the structure, electronic and topological properties of oxygen functionalized InSe and TlTe are studied. With the increased concentrations of oxygen coverage, the $InSeO_{0.25}$, $InSeO_{0.5}$ and $InSeO_{0.75}$, experience the transformation from indirect bandgap semiconductor to direct bandgap semiconductor and finally to QSH insulator. The nontrivial bandgap of InSeO is 0.121 eV, which owns potential applications at room temperature. The oxygen functionalized TlTe shows the same trend as the oxygen functionalized InSe. Due to the stronger SOC, the nontrivial bandgap of TlTeO is increased to 0.169 eV. In addition, the QSH phases in oxygen functionalized InSe and TlTe are derived from SOC induced p–p bandgap opening. Significantly, the QSH phases can be maintained in excess of 75% oxygen coverage and are robustly against the external strain, making the QSH effect easy to be achieved experimentally. Thus, the oxygen functionalized InSe and TlTe are fine candidate materials for the design and fabrication of the topological device.

Conflicts of interest

There are no conflicts to declare.

Acknowledgements

This work was supported by the National Natural Science Foundation of China (Grant No. 11904314), the Sailing Plan Project of Yibin University (No. 412-2021QH06, 412-2021QH08, 2018RC18, 2022PY18) and the Open Research Fund of Key Laboratory of Computational Physics of Sichuan Province (No. 412-2020JSWLZD008, JSWL2018KF01).

References

1 K. Xu, L. Yin, Y. Huang, T. A. Shifa, J. Chu, F. Wang, R. Cheng, Z. Wang and J. He, *Nanoscale*, 2016, **8**, 16802.
2 R. M. A. Lieth and J. C. J. M. Terhell, *Transition Metal Dichalcogenides*, Springer Press, Dordrecht, 1977.
3 S. Lei, F. Wen, L. Ge, S. Najmaei, A. George, Y. Gong, W. Gao, Z. Jin, B. Li, J. Lou, J. Kono, R. Vajtai, P. Ajayan and N. J. Halas, *Nano Lett.*, 2015, **15**, 3048.
4 P. A. Hu, L. Wang, M. Yoon, J. Zhang, W. Feng, X. Wang, Z. Wen, J. C. Idrobo, Y. Miyamoto, D. B. Geohegan and K. Xiao, *Nano Lett.*, 2013, **13**, 1649.
5 S. Lei, L. Ge, Z. Liu, S. Najmaei, G. Shi, G. You, J. Lou, R. Vajtai and P. M. Ajayan, *Nano Lett.*, 2013, **13**, 2777.
6 S. Sucharitakul, N. J. Goble, U. R. Kumar, R. Sankar, Z. A. Bogorad, F. C. Chou, Y. T. Chen and X. P. A. Gao, *Nano Lett.*, 2015, **15**, 3815.
7 D. A. Bandurin, A. V. Tyurnina, G. L. Yu, A. Mishchenko, V. Zólyomi, S. V. Morozov, R. K. Kumar, R. V. Gorbachev, Z. R. Kudrynskyi, S. Pezzini, Z. D. Kovalyuk, U. Zeitler, K. S. Novoselov, A. Patanè, L. Eaves, I. V. Grigorieva, V. I. Falko, A. K. Geim and Y. Cao, *Nat. Nanotechnol.*, 2017, **12**, 223.
8 D. J. Late, B. Liu, J. Luo, A. Yan, H. S. S. R. Matte, M. Grayson, C. N. R. Rao and V. P. Dravid, *Adv. Mater.*, 2012, **24**, 3549.
9 F. Liu, H. Shimotani, H. Shang, T. Kanagasekaran, V. Zólyomi, N. Drummond, V. I. Falko and K. Tanigaki, *ACS Nano*, 2014, **8**, 752.
10 S. R. Tamalampudi, Y. Y. Lu, U. R. Kumar, R. Sankar, C. D. Liao, B. K. Moorthy, C. H. Cheng, F. C. Chou and Y. T. Chen, *Nano Lett.*, 2014, **14**, 2800.
11 J. A. Olmos-Asar, C. R. Leão and A. Fazzio, *J. Appl. Phys.*, 2018, **124**, 045104.
12 G. Han, Z. G. Chen, J. Drennan and J. Zhou, *Small*, 2014, **14**, 2747.
13 Y. Guo, S. Zhou, Y. Bai and J. Zhao, *Appl. Phys. Lett.*, 2017, **110**, 163102.
14 A. Harvey, C. Backes, Z. Gholamvand, D. Hanlon, D. McAteer, H. C. Nerl, E. McGuire, A. Seral-Ascaso, Q. M. Ramasse, N. McEvoy, S. Winters, N. C. Berner, D. McCloskey, J. F. Donegan, G. S. Duesberg, V. Nicolosi and J. N. Coleman, *Chem. Mater.*, 2015, **27**, 3483.
15 C. L. Kane and E. J. Mele, *Phys. Rev. Lett.*, 2005, **95**, 146802.
16 C. L. Kane and E. J. Mele, *Phys. Rev. Lett.*, 2005, **95**, 226801.
17 M. König, S. Wiedmann, C. Brüne, A. Roth, H. Buhmann, L. W. Molenkamp, X. L. Qi and S. C. Zhang, *Science*, 2007, **318**, 766.
18 B. A. Bernevig, T. L. Hughes and S. C. Zhang, *Science*, 2006, **314**, 1757.
19 I. Knez, R. R. Du and G. Sullivan, *Phys. Rev. Lett.*, 2011, **107**, 136603.
20 C. Liu, T. L. Hughes, X. L. Qi, K. Wang and S. C. Zhang, *Phys. Rev. Lett.*, 2008, **100**, 236601.
21 H. B. Shu, *Eur. Phys. J. Plus*, 2022, **137**, 1225.
22 H. B. Shu and X. M. Liu, *Appl. Surf. Sci.*, 2022, **605**, 154591.
23 H. B. Shu, *Phys. Chem. Chem. Phys.*, 2021, **23**, 18951–18957.
24 H. B. Shu, X. H. Niu, X. J. Ding and Y. Wang, *Appl. Surf. Sci.*, 2019, **479**, 475–481.
25 J. E. Padilha, L. B. Abdalla, A. J. R. da Silva and A. Fazzio, *Phys. Rev. B*, 2016, **93**, 045135.
26 R. W. Zhang, W. X. Ji, C. W. Zhang, P. Li and P. J. Wang, *Phys. Chem. Chem. Phys.*, 2016, **18**, 28134.
27 X. Chen, L. Li and M. Zhao, *Phys. Chem. Chem. Phys.*, 2015, **17**, 16624.
28 Y. Xu, B. Yan, H. J. Zhang, J. Wang, G. Xu, P. Tang, W. Duan and S. C. Zhang, *Phys. Rev. Lett.*, 2013, **111**, 136804.
29 G. Yang, Z. Xu, Z. Liu, S. Jin, H. Zhang and Z. Ding, *J. Phys. Chem. C*, 2017, **121**, 12945.
30 J. Zhao, W. Guo and J. Ma, *Nano Res.*, 2017, **10**, 491.
31 Q. Zhang and U. Schwingenschlögl, *Phys. Rev. B*, 2016, **93**, 045312.
32 Z. Song, C. C. Liu, J. Yang, J. Han, M. Ye, B. Fu, Y. Yang, Q. Niu, J. Lu and Y. Yao, *NPG Asia Mater.*, 2014, **6**, e147.
33 R. R. Q. Freitas, R. Rivelino, F. de Brito Mota and C. M. C. de Castilho, *J. Phys. Chem. C*, 2015, **119**, 23599.
34 Y. Ma, L. Kou, A. Du and T. Heine, *Nano Res.*, 2015, **8**, 3412.
35 R. Juarez-Mosqueda, Y. Ma and T. Heine, *Phys. Chem. Chem. Phys.*, 2016, **18**, 3669.
36 Y. Z. Jia, W. X. Ji, C. W. Zhang, P. Li, M. J. Ren and P. J. Wang, *J. Mater. Chem. C*, 2016, **4**, 8750.
37 L. Li, O. Leenaerts, X. Kong, X. Chen, M. Zhao and F. M. Peeters, *Nano Res.*, 2017, **10**, 2168.
38 Y. Ma, X. Li, L. Kou, B. Yan, C. Niu, Y. Dai and T. Heine, *Phys. Rev. B*, 2015, **91**, 235306.
39 R. R. Q. Freitas, F. de Brito Mota, R. Rivelino, C. M. C. de Castilho, A. Kakanakova-Georgieva and G. K. Gueorguiev, *Nanotechnology*, 2016, **27**, 055704.
40 C. P. Crisostomo, L. Z. Yao, Z. Q. Huang, C. H. Hsu, F. C. Chuang, H. Lin, M. A. Albao and A. Bansil, *Nano Lett.*, 2015, **15**, 6568.
41 Y. P. Wang, W. X. Ji, C. W. Zhang, P. Li, F. Li, P. J. Wang, S. S. Li and S. S. Yan, *Appl. Phys. Lett.*, 2016, **108**, 073104.
42 H. Zhao, W. X. Ji, C. W. Zhang, P. Li, S. F. Zhang, F. Li, P. J. Wang, S. S. Li and S. S. Yan, *J. Mater. Chem. C*, 2017, **5**, 2656.
43 D. Wang, L. Chen, C. Shi, X. Wang, G. Cui, P. Zhang and Y. Chen, *New J. Phys.*, 2016, **18**, 033026.
44 L. Kou, H. Fu, Y. Ma, B. Yan, T. Liao, A. Du and C. Chen, *Phys. Rev. B*, 2018, **97**, 075429.
45 R. W. Zhang, C. W. Zhang, W. X. Ji, S. S. Li, S. S. Yan, S. J. Hu, P. Li, P. J. Wang and F. Li, *Sci. Rep.*, 2016, **6**, 18879.

46 Y. P. Wang, W. X. Ji, C. W. Zhang, P. Li, S. F. Zhang, P. J. Wang, S. S. Li and S. S. Yan, *Appl. Phys. Lett.*, 2017, **110**, 213101.
47 S. Zhang, W. Zhou, Y. Ma, J. Ji, B. Cai, S. A. Yang, Z. Zhu, Z. Chen and H. Zeng, *Nano Lett.*, 2017, **17**, 3434.
48 Y. P. Wang, S. S. Li, W. X. Ji, C. W. Zhang, P. Li and P. J. Wang, *J. Phys.: Condens. Matter*, 2018, **30**, 105303.
49 N. Balakrishnan, Z. R. Kudrynskyi, E. F. Smith, M. W. Fay, O. Makarovsky, Z. D. Kovalyuk, L. Eaves, P. H. Beton and A. Patanè, *2D Mater.*, 2017, **4**, 025043.
50 O. D. Pozo-Zamudio, S. Schwarz, M. Sich, I. A. Akimov, M. Bayer, R. C. Schofield, E. A. Chekhovich, B. J. Robinson, N. D. Kay, O. V. Kolosov, A. I. Dmitriev, G. V. Lashkarev, D. N. Borisenko, N. N. Kolesnikov and A. I. Tartakovskii, *2D Mater.*, 2015, **2**, 035010.
51 T. E. Beechem, B. M. Kowalski, M. T. Brumbach, A. E. McDonald, C. D. Spataru, S. W. Howell, T. Ohta, J. A. Pask and N. G. Kalugin, *Appl. Phys. Lett.*, 2015, **107**, 173103.
52 S. Zhou, C. C. Liu, J. Zhao and Y. Yao, *npj Quantum Mater.*, 2018, **3**, 16.
53 G. Kresse and J. Furthmuller, *Phys. Rev. B: Condens. Matter Mater. Phys.*, 1996, **54**, 11169.
54 G. Kresse and D. Joubert, *Phys. Rev. B: Condens. Matter Mater. Phys.*, 1999, **59**, 1758.
55 J. P. Perdew, K. Burke and M. Ernzerhof, *Phys. Rev. Lett.*, 1996, **77**, 3865.
56 H. J. Monkhorst and J. D. Pack, *Phys. Rev. B: Condens. Matter Mater. Phys.*, 1976, **13**, 5188.
57 X. Gonze and C. Lee, *Phys. Rev. B: Condens. Matter Mater. Phys.*, 1997, **55**, 10355.
58 A. A. Mostofi, J. R. Yates, Y. S. Lee, I. Souza, D. Vanderbilt and N. Marzari, *Comput. Phys. Commun.*, 2008, **178**, 685.
59 Q. S. Wu, S. N. Zhang, H. F. Song, M. Troyer and A. A. Soluyanov, *Comput. Phys. Commun.*, 2017, **224**, 405.
60 Z. F. Wang, K. H. Jin and F. Liu, *Nat. Commun.*, 2016, **7**, 12746.
61 Q. F. Liang, R. Yu, J. Zhou and X. Hu, *Phys. Rev. B*, 2016, **93**, 035135.
62 C. Li, K. H. Jin, S. Zhang, F. Wang, Y. Jia and F. Liu, *Nanoscale*, 2018, **10**, 5496.
63 J. Heyd, G. E. Scuseria and M. Ernzerhof, *J. Chem. Phys.*, 2003, **118**, 8207.
64 M. Z. Hossain, J. E. Johns, K. H. Bevan, H. J. Karmel, Y. T. Liang, S. Yoshimoto, K. Mukai, T. Koitaya, J. Yoshinobu, M. Kawai, A. M. Lear, L. L. Kesmodel, S. L. Tait and M. C. Hersam, *Nat. Chem.*, 2012, **4**, 305.
65 R. Yu, X. L. Qi, A. Bernevig, Z. Fang and X. Dai, *Phys. Rev. B: Condens. Matter Mater. Phys.*, 2011, **84**, 075119.
66 X. L. Qi and S. C. Zhang, *Rev. Mod. Phys.*, 2011, **83**, 1057.
67 J. J. Zhou, W. Feng, C. C. Liu, S. Guan and Y. Yao, *Nano Lett.*, 2014, **14**, 4767.
68 P. F. Liu, L. Zhou, T. Frauenheim and L. M. Wu, *Nanoscale*, 2017, **9**, 1007.
69 T. H. Hsieh, H. Lin, J. W. Liu, W. H. Duan, A. Bansil and L. Fu, *Nat. Commun.*, 2012, **3**, 982.
70 H. B. Shu, *J. Mater. Chem. C*, 2021, **9**, 4505–4513.
71 H. B. Shu, *Appl. Surf. Sci.*, 2021, **559**, 149956.
72 H. B. Shu, M. L. Zhao and M. L. Sun, *ACS Appl. Nano Mater.*, 2019, **2**, 6482–6491.
73 H. B. Shu, Y. H. Li, X. H. Niu and J. Y. Guo, *J. Mater. Chem. C*, 2018, **6**, 83–90.